Electronic Supplementary Material (ESI) for Environmental Science: Nano.

Supporting Information

Super stable evaporators based on upcycled self-healing adsorbents for wastewater regeneration

Meng Li[a,#], Hongmin Guo[a,#], Yumeng Xiao[a], Sichen Liu[a], Yifan Lu[a], Lidong Wang[a,] and Tony D. James[b,c,]**

[a]*Hebei Key Lab of Power Plant Flue Gas Multi-Pollutants Control, Department of Environmental Science and Engineering, North China Electric Power University, Baoding, 071003, PR China*

[b]*Department of Chemistry, University of Bath, Bath, BA2 7AY, UK, School of Chemistry and Chemical Engineering*

[c]*Henan Normal University, Xinxiang 453007, P. R. China*

# indicates the co-first author.

*Corresponding author E-mail: wld@ncepu.edu.cn; t.d.james@bath.ac.uk

1.Experimental Section

1.1. Chemicals and materials

Carboxymethylated nanocellulose (C-CNC) was purchased from Aladdin Chemical Reagent Co., Ltd. (Shanghai, China). Hydrochloric acid (HCl) was of analytical grade and were obtained from Tianjin Damao Chemical Reagent Factory. Ammonium persulfate (APS), Disodium tetraborate decahydrate (Borax), Poly(vinyl alcohol) (PVA) were obtained from Tianjin Kermel Reagent Co., Ltd. Deionized water (DI-water) was produced by RO-400G Standard ultrapure water system and used in all experiments. All of chemicals were used in this paper without further purification.

Materials Characterization

Transmission electron microscopy (TEM) images were captured with a JEM2100F transmission electron microscope. Fourier transform infrared (FTIR) spectra were acquired using the Thermo Electron Nicolet iZ10 spectrometer within the spectral range of 4500-500 The sample morphology was assessed through scanning electron microscopy (SEM) ying the Hitachi-s4800 instrument. Zeta potentials of C-CNC, PANI, CNC-PANI, CPPB gel in ethyl alcohol (0.01 wt%) were determined using a Nano ZS Malvern Zetasizer. The concentration of heavy mental ions were determined by an inductively 11 coupled plasma optical emission spectrometer (ICP-OES, PE-7000DV, USA). Absorption spectra and reflectance were conducted using a UV-vis-NIR spectrometer (Cary 5000) with an integrating sphere unit and automation of reflectance measurement unit, and the measurements were corrected by baseline/blank correction with dark correction.

Mechanical property

test was carried out by universal testing machine (Instron 5943) at room temperature. The stress (σ) -strain (ε) measurements were made for a rectangular hydrogel sample with a width of 10 mm, a depth of 4 mm and a length of 30 mm. The fixed drawing rate was 50 mm /min and the initial distance between the two fixtures was 10 mm.

Self-healing property

-healing performance was assessed using a universal testing machine. A rectangular hydrogel sample (10 mm in width, 4 mm in depth, and 30 mm in length) was bisected with a blade, and the two separate sections were subsequently brought into immediate contact without applying additional stress or external stimuli at the interface. Following the self-healing process, stress (σ) and strain (ε) measurements were once again conducted on the healed hydrogel sample. The stress healing efficiency (HE), defined as the ratio of tensile

strength between the original hydrogel and the healed hydrogel, was then calculated by Eq. (1)[1]

$$HE(stress\ healing\ efficiency) = \left[\frac{F(healed)}{F(original)}\right] * 100\% \quad (1)$$

Here, F(original) and F(healed) represent the tensile strength of the original and healed samples, respectively, as determined from the stress-strain curves.

Self-adhesive properties

was tested by adhering samples (30 mm wide, 4 mm deep and 30 mm long) to surfaces on different substrates (wood sponges, commercial sponges and cotton threads).

Calculations Related to Solar Water Evaporation

gy efficiency (η) was determined using Eq. (2) as follows[2]:

$$\eta = \frac{mh_{LV}}{C_{opt}qi} \quad (2)$$

Here, η signifies the energy efficiency, while m denotes the mass flux under steady-state conditions. The symbol h_{LV} represents the vaporization enthalpy of the water in the samples, specifically set at 2444 J g^{-1}, with no consideration for sensible heat.[3]; C_{opt} stands for optical concentration, while qi represents the solar irradiation power incident on the adsorber surface, measured at 100 mW cm^{-2}.

The water content (Qs) is represented by Eq. (3)[4]

$$Q_s = {}^{W}/_{W_d} \quad (3)$$

where W and W_d are the weights of the water in the swollen sample and the corresponding dried aerogel sample, respectively.

The water transport rate (V) can be calculated by Eq. (4)[5]

$$V = Q_s/t \quad (4)$$

where t is the half-swollen time.

Simulated wastewater

ssess the feasibility of applying CPPB gel in the enrichment of metal ions, a simulation of actual industrial wastewater was conducted. The simulated wastewater contained various heavy metals at concentrations indicated in Table S1, while the pH of the simulated wastewater was set at 6.5.[2]

Table S1. Identification and quantification of heavy metal species and concentrations in simulated wastewater

Metal ion	Concentration (ppb)
Cu^{2+}	2900.0
Pb^{2+}	190.0
Cd^{2+}	80.0
Hg^{2+}	16.5

The concentration of organic dyes MB and MO was 10 ppm.[6]

1.8. Energy calculation

In an effort to explain the extremely efficient utilization of the solar energy by the CPPB evaporator, we conducted an in-depth analysis of energy losses using the following equation[7]:

$$Q_{sun} = Q_{eavp} + Q_{loss} = S_{eavp} D_a h_{fg} \left(C_{sat}(T_s) - \oint_{\infty} C_{sat}(T_{\infty}) \right) + A h_{loss} \Delta T \quad (5)$$

$$A \partial q_{solar}^{"} = S_{eavp} D_a h_{fg} \Delta c + A \varepsilon \sigma \left({T_s}^4 - {T_{\infty}}^4 \right) + A h_{conv} + \Delta T + \frac{\Delta T}{\frac{1}{S_{cond} K_1} + \frac{t_s}{A K_{wick}}} \quad (6)$$

In the equation(5), where S_{evap}, D_a, and A are the evaporative shape factor, vapor mass diffusivity in air, area of the evaporator, respectively. Csat(T_s) and Csat(T_∞) are vapor saturation concentrations at T_s and T_∞, respectively. $\oint_{\infty}$ is the far-field relative humidity.

In the equation(6), where ∂, ε, σ, h_{conv}, K_1, and K_{wick} are the evaporator solar absorptance, evaporator infrared emissivity, Stefan‑Boltzmann constant, convective heat loss coefficient, water thermal conductivity, and effective thermal conductivity of the capillary wick, respectively. S_{cond} = 2D is the conductive shape factor for a circular-disk evaporator. h_{conv} = $1/(1/h_a + 1/h_c)$ includes the contributions of both the heat transfer coefficient of air ambient (h_a) and convection cover (h_c).

For the CPPB evaporator, A_{top} is 4 cm^2, T_{top} is 35.8 °C, A_{side} is 6.4 cm^2, and T_{side} is 30.5 °C, A_{cotton} is141.92 cm^2, T_{cotton} is 23.6℃, $T_{environment}$ is the ambient temperature (25 °C), ε is emissivity of the absorbing surface (~0.98), σ is the Stefan-Boltzmann constant (5.67×10^{-8} W m^{-2} K^{-4}), h is convection heat transfer coefficient (assumed to be 5 W m^{-2} K^{-1}), Since the side evaporation surface has a lower temperature than the environment temperature, it could gain energy from the environment.

According to the above equation, for the CPPB evaporator, the radiation loss from the top

evaporation surface was estimated to be 0.0268 W, the radiation energy loss of the side evaporation surface was 0.0213 W, while radiation energy gain of the cotton side evaporation surface from surrounding environment was 0.0237 W; Convection loss from the top evaporation surface was estimated to be 0.0216 W, convection loss from the side evaporation surface was estimated to be 0.0176 W and convection energy gain of the cotton side evaporation surface from surrounding environment was estimated to be 0.0993 W.

Therefore, the evaporator has a net energy gain of 0.0357 W from the environment.

1.9. The Solar-to-Vapor Conversion Efficiency

The heat transfer process of solar vapor generation includes four energy flows, that is, solar energy input (Q_{solar}), heat exchange with the environment (Q_{top} + Q_{side}), vapor output under 1 kW m^{-2} ($Q_{eva,1\ sun}$), and dark conditions ($Q_{eva,dark}$), respectively. Thus, the energy transfer process of our evaporation device can be expressed as the following equations[8]:

$$Q_{solar} = Q_{eva,1sun} + Q_{eva,dark} + Q_{top} + Q_{side} \quad (7)$$

$$\eta_{eva,1sun} = 1 - \frac{Q_{top}}{Q_{solar}} - \frac{Q_{side}}{Q_{solar}} - \frac{Q_{eva,dark}}{Q_{solar}} = 1 - \eta_{top} - \eta_{side} - \eta_{eva,dark} \quad (8)$$

$$\eta_{top} = \frac{hA\Delta T}{Q_{solar}} + \frac{\varepsilon A\sigma\left(T_1{}^4 - T_2{}^4\right)}{Q_{solar}} + cm\Delta T/Q_{solar} \quad (9)$$

$$\eta_{eva,dark} = (m_1 - m_2) * \eta/Q_{solar} \quad (10)$$

$$Q_{side} = 4 \int_{Tside(b) \le T\infty} A_{side} h_{conv}(T_{side}(b) - T_\infty) d_b + 4\partial_{side}\sigma \int_{Tside(b) \le T\infty} A_{side}(T_{side}{}^4(b) - T_\infty{}^4) d_b \quad (11)$$

$$\eta_{side} = Q_{side}/Q_{solar} \quad (12)$$

1.10. Theoretical simulation

1.10.1. COMSOL Simulation of temperature distribution in SG3 evaporator.

Initially, a simulated 3D model with identical size parameters to that of SG3 evaporator was constructed, that is, a gel made of CPPB with dimensions of 1 cm by 1 cm and a thickness of 0.5 mm. The gel will be connected to a cotton thread with a diameter of 4 mm and a length of 16 cm, and the cotton thread will be in contact with water. Coupled with the heat transfer physical field, the natural convection temperature distribution in the air region after absorbing radiant heat from light on the top surface is obtained, and the overall temperature conservation

Could be described by the equation as given below:

$$\rho C_p u \nabla T + \nabla q = Q + Q_p + Q_{vd} \quad (13)$$

$$q = -k\nabla T \quad (14)$$

$$Q_p = \alpha_p T\left(\frac{\partial p}{\partial t} + u\nabla p\right) \quad (15)$$

$$Q_{vd} = \tau{:}\nabla u \quad (16)$$

Where the ρ is the density (SI unit: kg/m^3); C_p is the specific heat capacity at constant pressure (SI unit: J/(kg·K)); T is the absolute temperature (SI unit: K); u is the velocity vector (SI unit: m/s); q is the heat flux by conduction (SI unit: W/m^2); Q contains heat sources other than viscous dissipation (SI unit: W/m^3)

On the surface of the curved pipe, the area that receives light is used to solve the heat power of the light using the deposition beam boundary, using Equation:

$$-nq = I_0 \frac{|e\ n|}{\|e\|} \quad (17)$$

Where the n represents the normal vector, e represents the direction of the light. I_0 represents the power density of the light, measured in watts per square meter (W/m^2). Lastly, q represents the surface heat flux.

The numerical simulations are conducted by COMSOL Multiphysics 5.4, under the steady and transient analysis mode. Wherein, a constant heat flux of 1 kW m^{-2} occurs on the top, corresponding to the solar energy input on the surface of the SG3. The convection heat transfer in the polymeric network was disabled to describe the water restriction effect. To carry out a qualitative analysis, it is assumed that the temperature of environment and water was set to 30 ºC (303 K); the balanced heat flux was 1 kW m^{-2}.

1.10.2. COMSOL Simulation of water transport in SG3 evaporator.

In the process of evaporation in a thin layer, water will flow in the form of a porous medium, which can be solved using the Brinkman equation. The Brinkman equation is based on Darcy's law and is used to solve the equation for saturated porous media. By setting the top evaporation rate as the outlet boundary condition, the overall velocity distribution and pressure distribution under the influence of gravity can be solved. Thus, it is calculated as follows:

$$0 = \nabla[-pI + K] - \left(\mu\kappa^{-1} + \beta\rho|u| + \frac{Q_m}{\varepsilon_p{}^2}\right)u + F + \rho g \quad (18)$$

$$\rho\nabla u = Q_m \quad (19)$$

Where the μ (SI unit: kg/(m·s)) is the dynamic viscosity of the fluid; u (SI unit: m/s) is the velocity vector; ρ (SI unit: kg/m^3) is the density of the fluid; p (SI unit: Pa) is the pressure; ε_p is

the porosity; κ (SI unit: m^2) is the permeability of the porous medium, and Q_m (SI unit: $kg/(m^3 \cdot s)$) is a mass source or sink; I is the identity matrix (unitless);

Supporting Figures

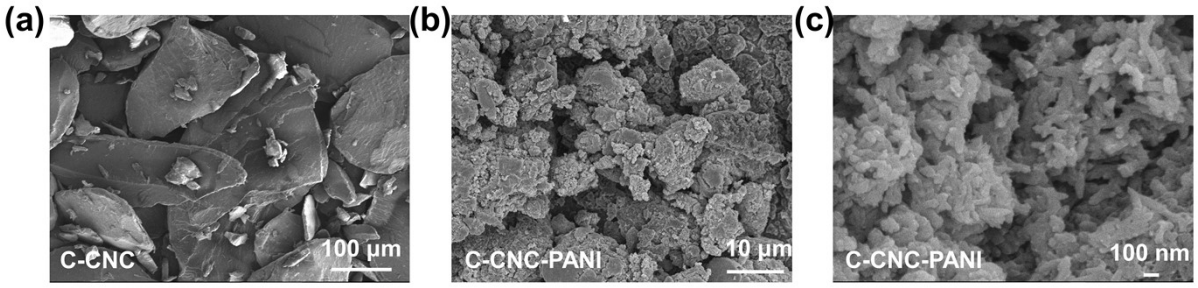

Figure S1 SEM images of C-CNC (a), C-CNC-PANI (b, c)

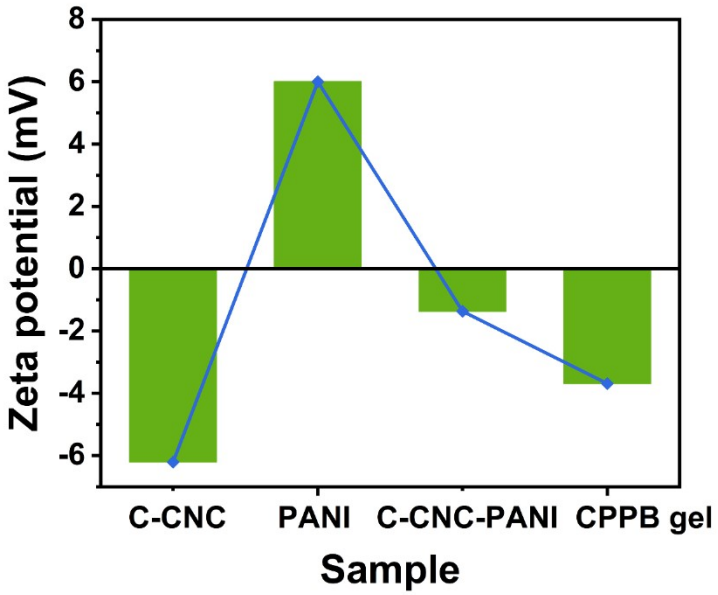

Figure S2 Zeta potential of C-CNC, PANI, C-CNC-PANI, CPPB gel.

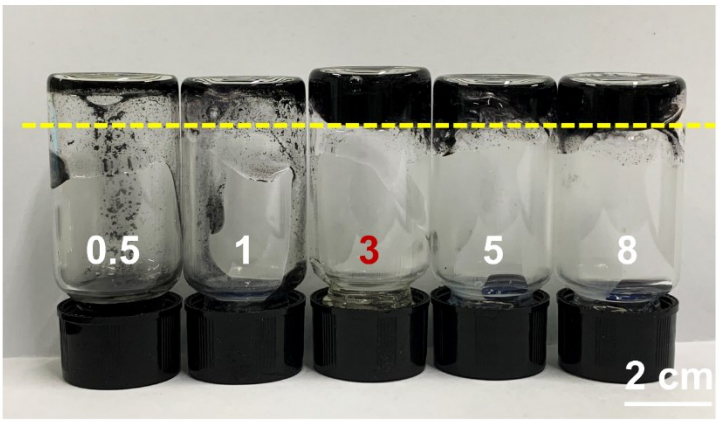

Figure S3 Gelation of borax in different proportions in CPPB gels (x wt% in water)

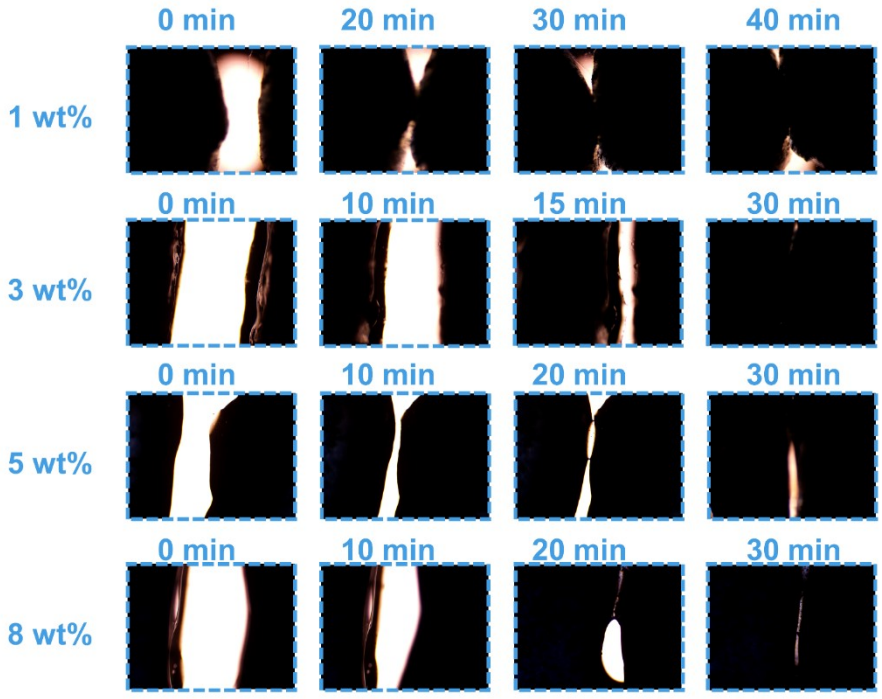

Figure S4 Self-healing process of CPPB hydrogels with different ratios of borax.

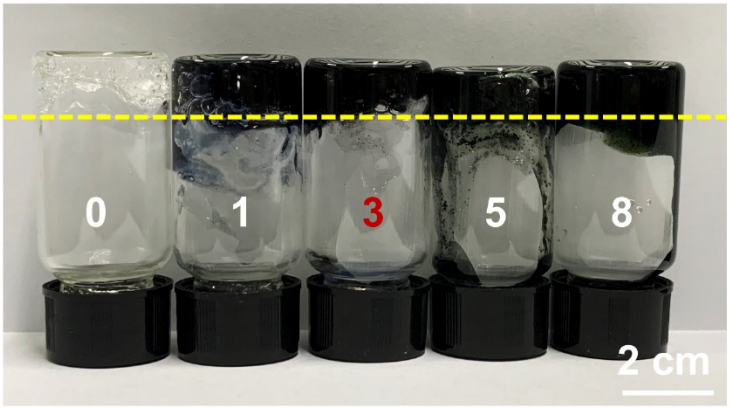

Figure S5 Gelation of C-CNC-PANI in different proportions in CPPB gels (x wt% in water)

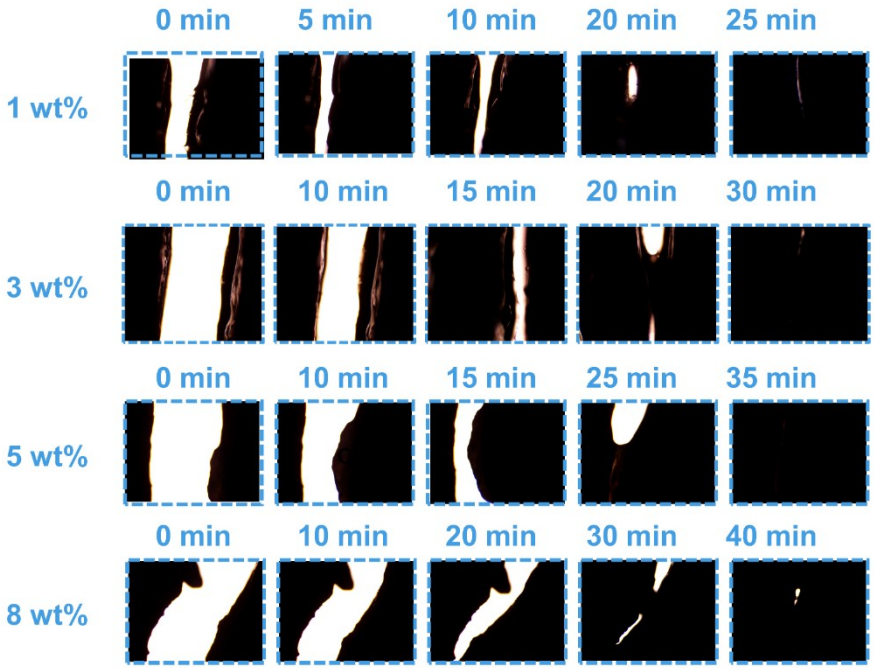

Figure S6 Self-healing process of CPPB hydrogels of different ratios of C-CNC-PANI.

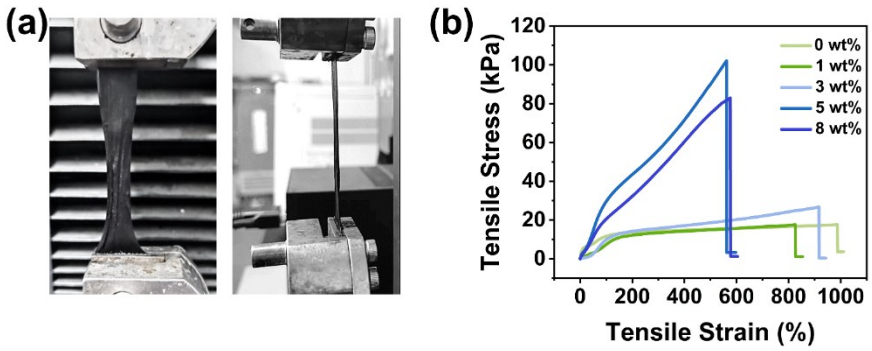

Figure S7 (a) Tensile test setup and specimens. (b) Tensile stress-strain curves of CPPB gels of different ratios of C-CNC-PANI.

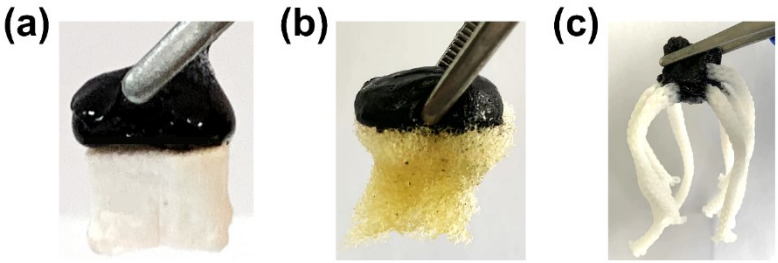

Figure S8 Self-adhesive properties were tested by adhering samples (30 mm wide, 4 mm deep and 30 mm long) to surfaces on different substrates (wood sponges (a), commercial sponges (b) and cotton threads(c)).

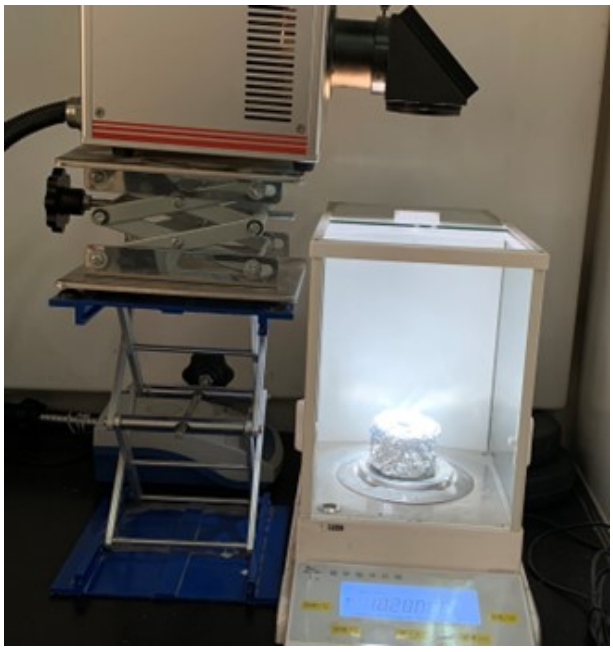

Figure S9 The photographs of home-built set-up for steam generation with the solar simulator.

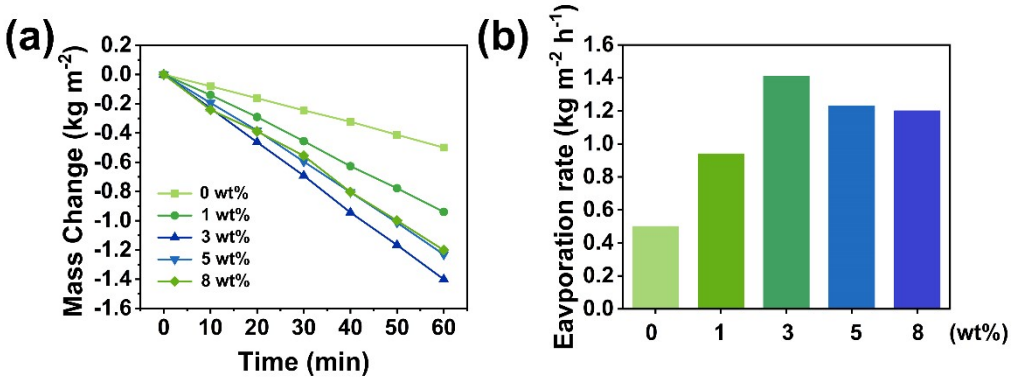

Figure S10 (a) The mass loss and (b) water evaporation rate of samples with varying ratios of C-CNC-PANI composites.

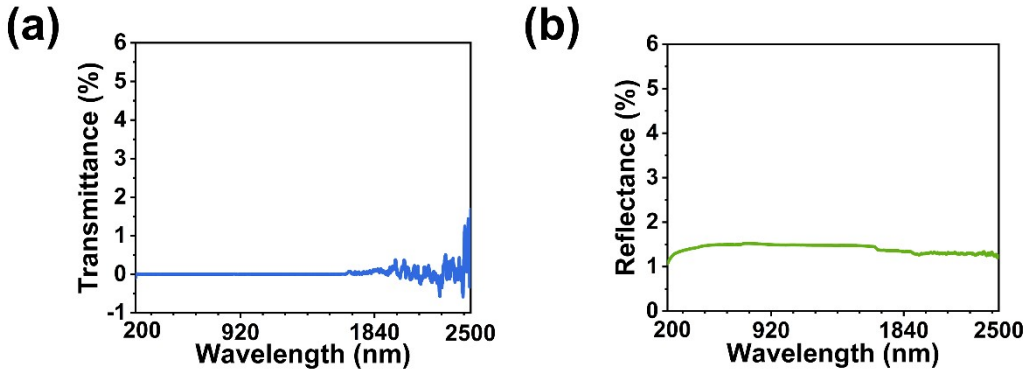

Figure S11 (a) Transmittance and (b) reflectance spectra of the CPPB gels in the wavelength range of 200-2500 nm.

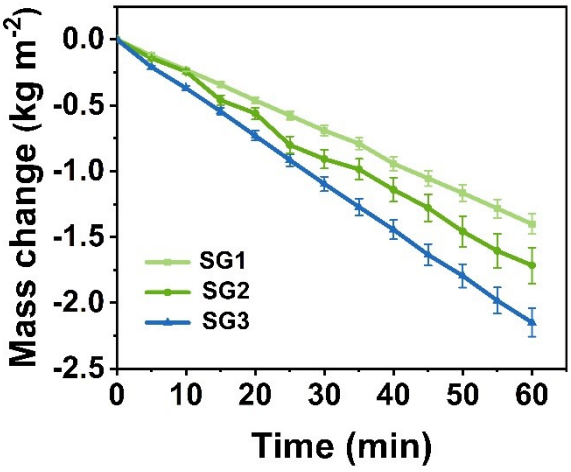

Figure S12 Mass change of water from SG1, SG2 and SG3 evaporations.

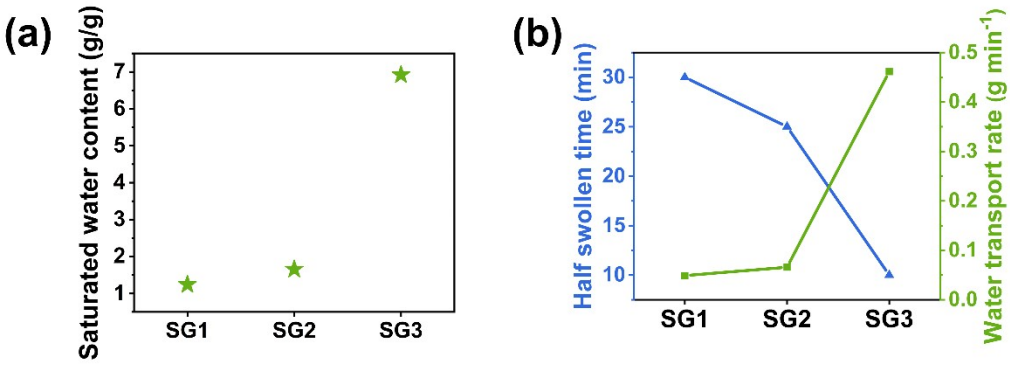

Figure S13 (a) Swollen time and the calculated water transport rate of SG1, SG2 and SG3 evaporations. (b) Saturated water content for three evaporators.

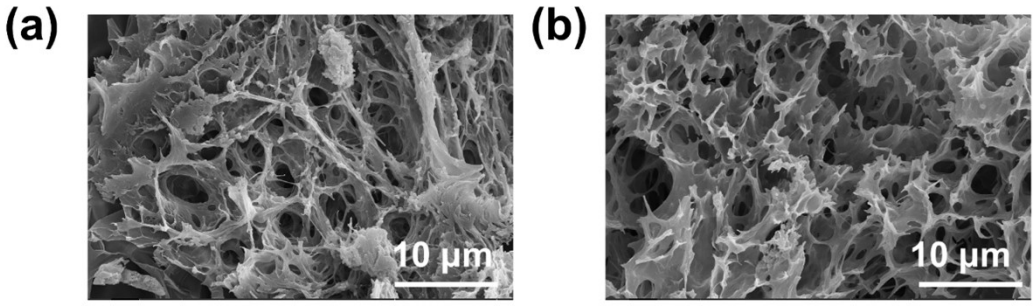

Figure S14 (a) SEM image of hydrogel before evaporation experiment. (b) SEM image of hydrogel after multiple evaporation experiment.

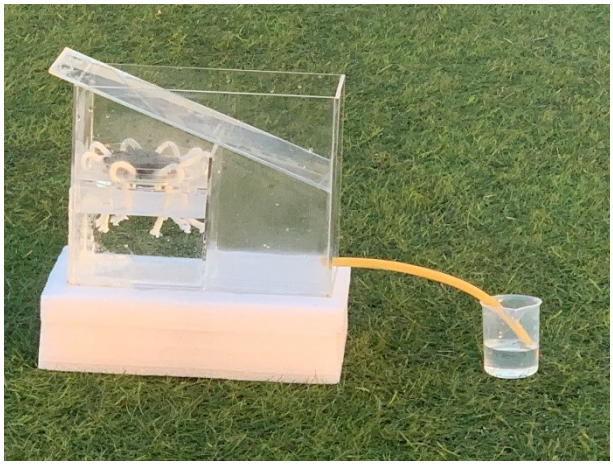

Figure S15 Image of solar steam generation setup under sunlight irradiation.

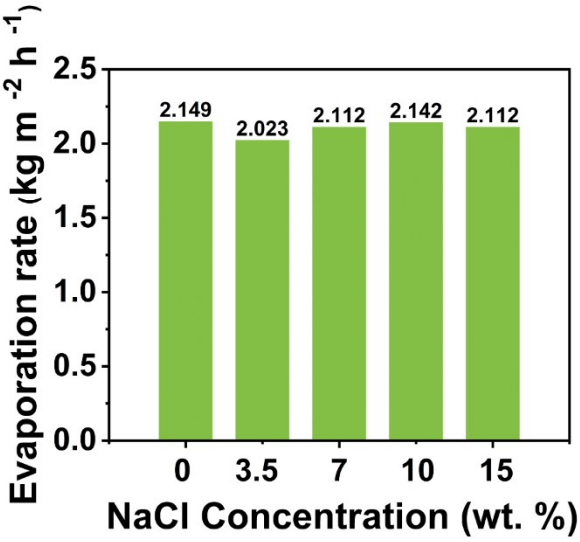

Figure S16 The water evaporation rate of SG3 evaporator with varying salt concentrations.

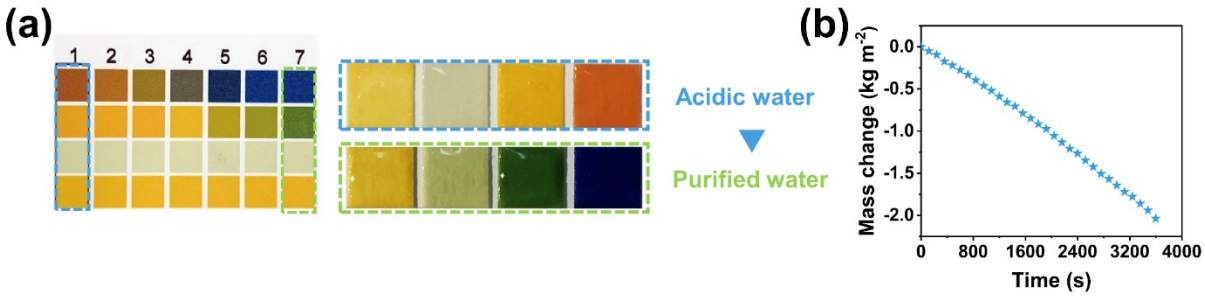

Figure S17 (a) The alteration in pH before and after the evaporation of a strong acidic solution. (b) The water evaporation rate in SG3 evaporator under highly acidic conditions.

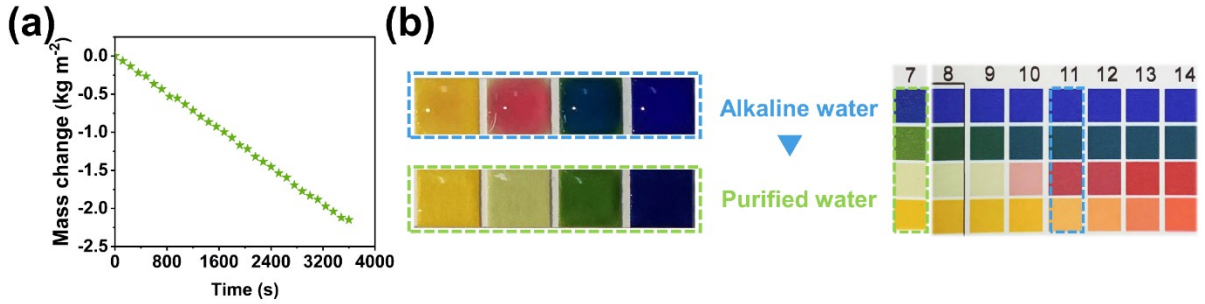

Figure S18 (a) The water evaporation rate in SG3 evaporator under highly alkaline conditions. (b) The alteration in pH before and after the evaporation of a strong alkaline solution.

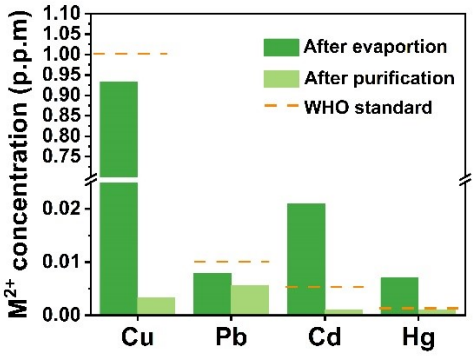

Figure S19 Comparison of heavy metal ion concentrations after evaporation and after purification exclusively for SG3 evaporator.

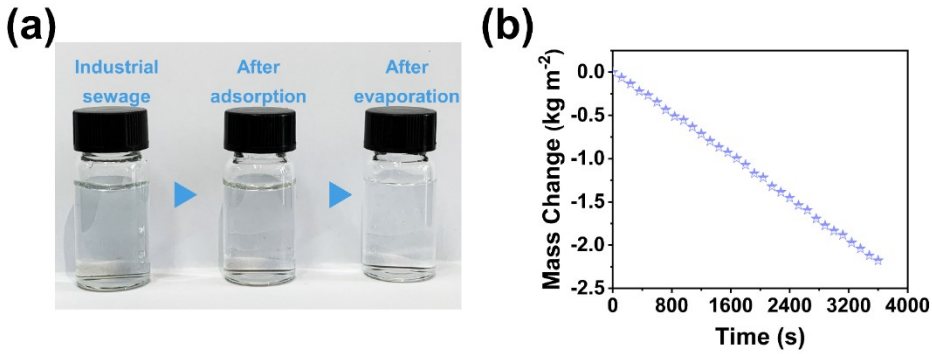

Figure S20 (a) The color changes in the solutions of the industrial sewage, the adsorbed solution, and the evaporated solution. (b) The evaporation rate of SG3 evaporator with industrial sewage.

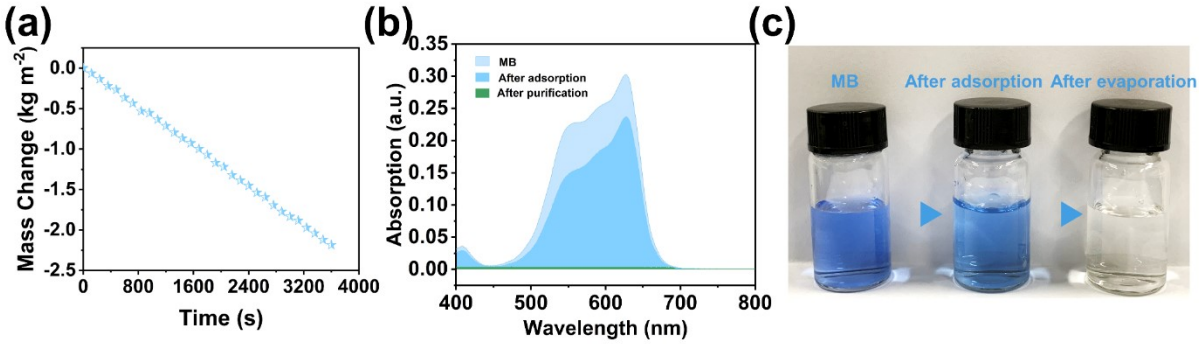

Figure S21 (a) The evaporation rate of SG3 evaporator in methylene blue (MB) solution. (b) Absorption spectra of MB, after adsorption solutions and the corresponding condensed pure water after evaporation. (c) The color changes in the solutions of the original MB, the MB adsorbed solution, and the evaporated MB solution.

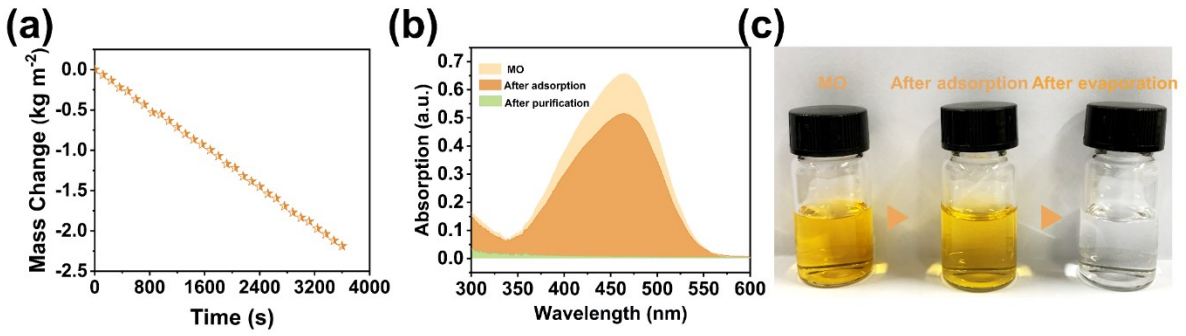

Figure S22 (a) The evaporation rate of SG3 evaporator in methyl orange (MO) solution. (b) Absorption spectra of MO, after adsorption solutions and the corresponding condensed pure water after evaporation. (c) The color changes in the solutions of the original MO, the MO adsorbed solution, and the evaporated MO solution.

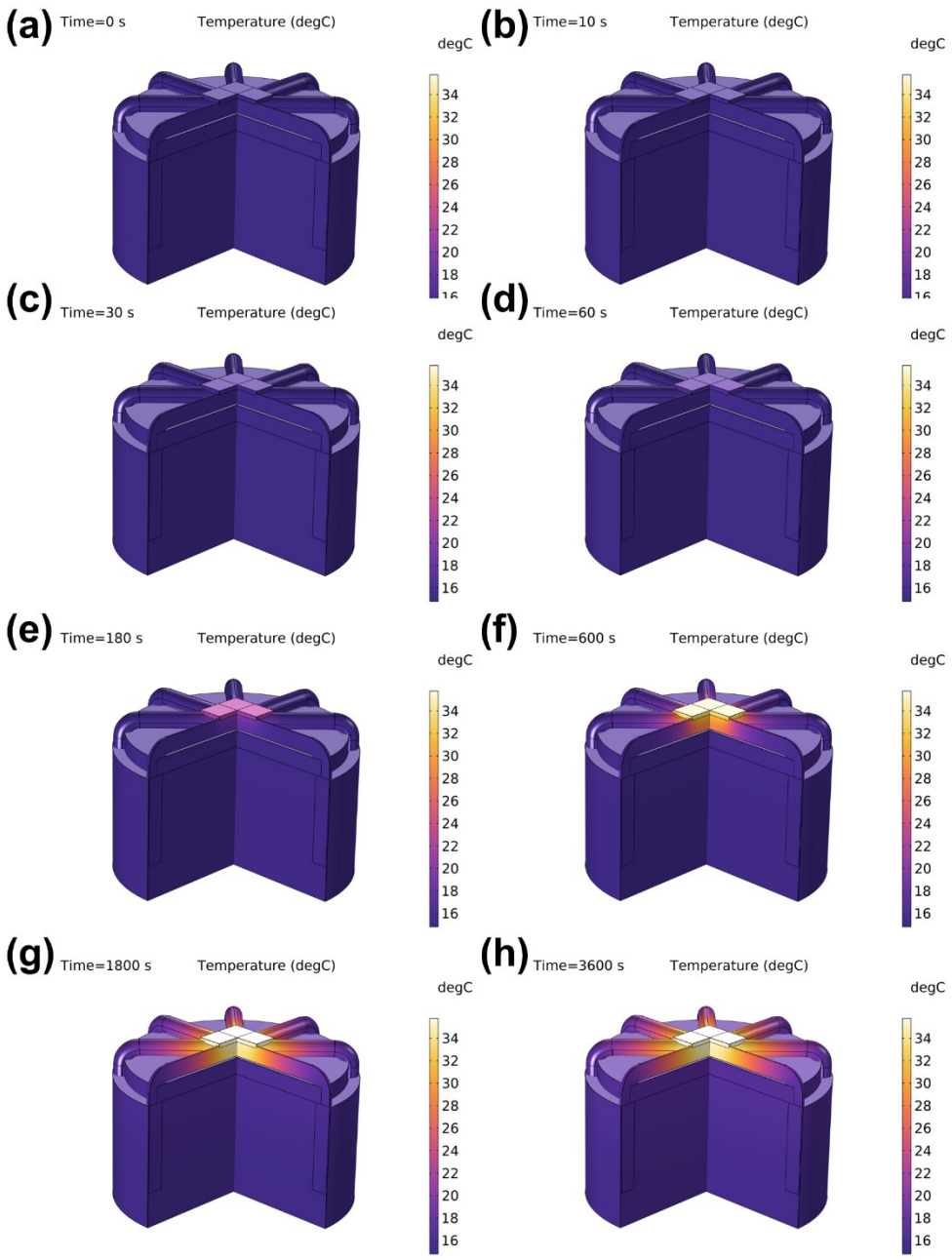

Figure S23 Transient state simulation of temperature distributions at (a) 0 s, (b) 10 s, (c) 30 s, (d) 60 s, (e) 180 s, (f) 600 s, (g) 1800 s and (h) 3600 s, respectively.

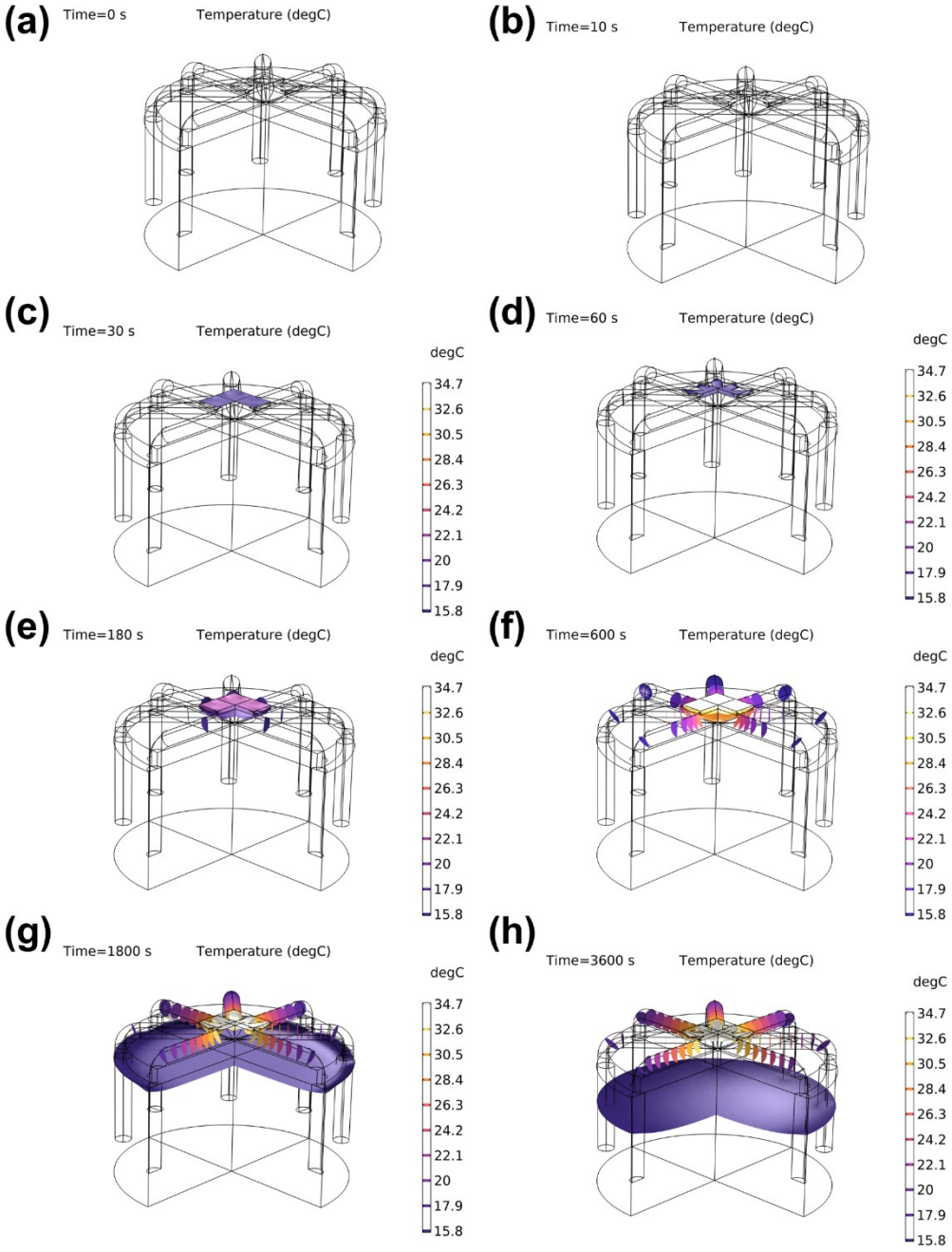

Figure S24 Transient state simulation of temperature isosurface at (a) 0 s, (b) 10 s, (c) 30 s, (d) 60 s, (e) 180 s, (f) 600 s, (g) 1800 s and (h) 3600 s, respectively.

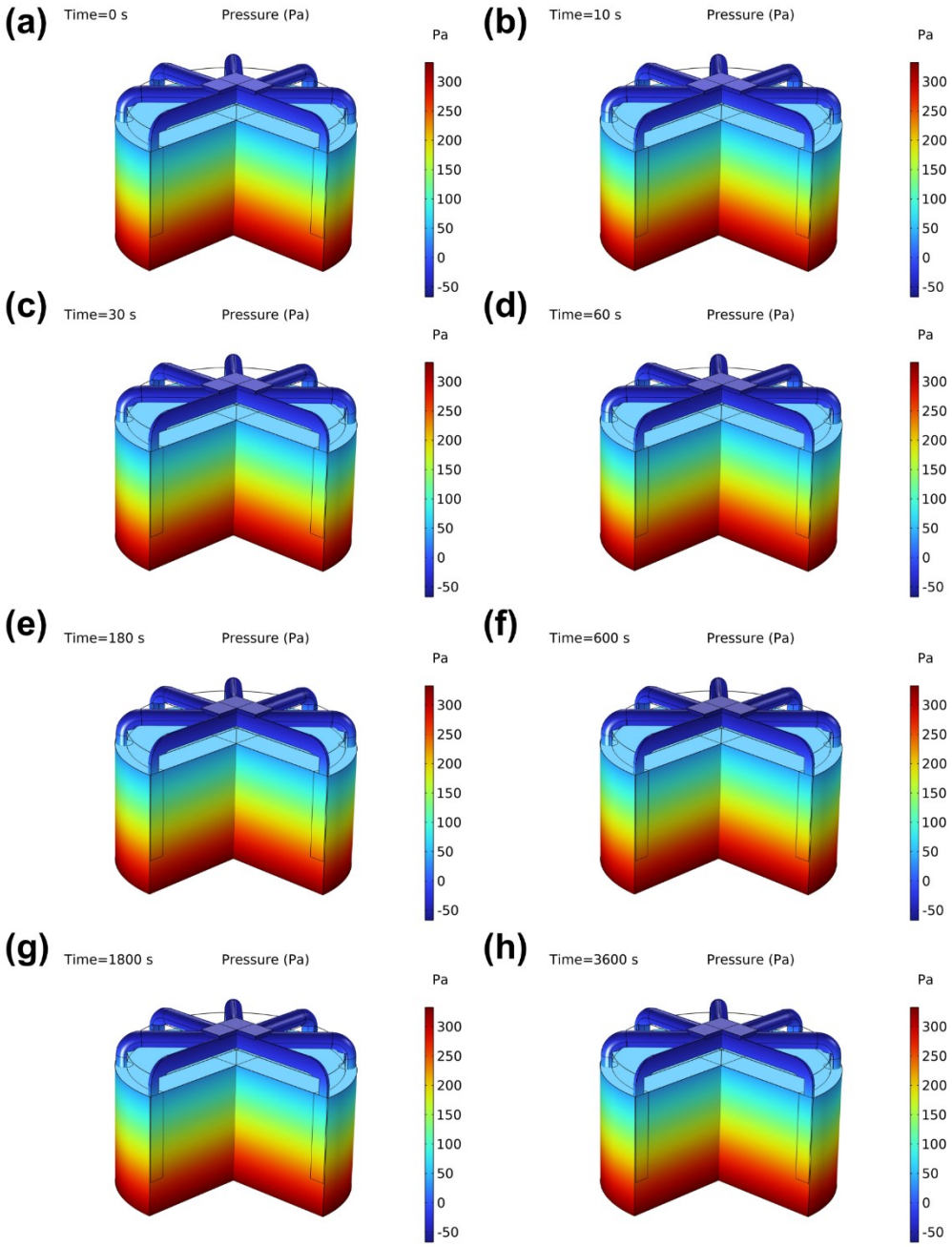

Figure S25 Transient simulation of relative water pressure distributions at (a) 0 s, (b) 10 s, (c) 30 s, (d) 60 s, (e) 180 s, (f) 600 s, (g) 1800 s and (h) 3600 s, respectively.

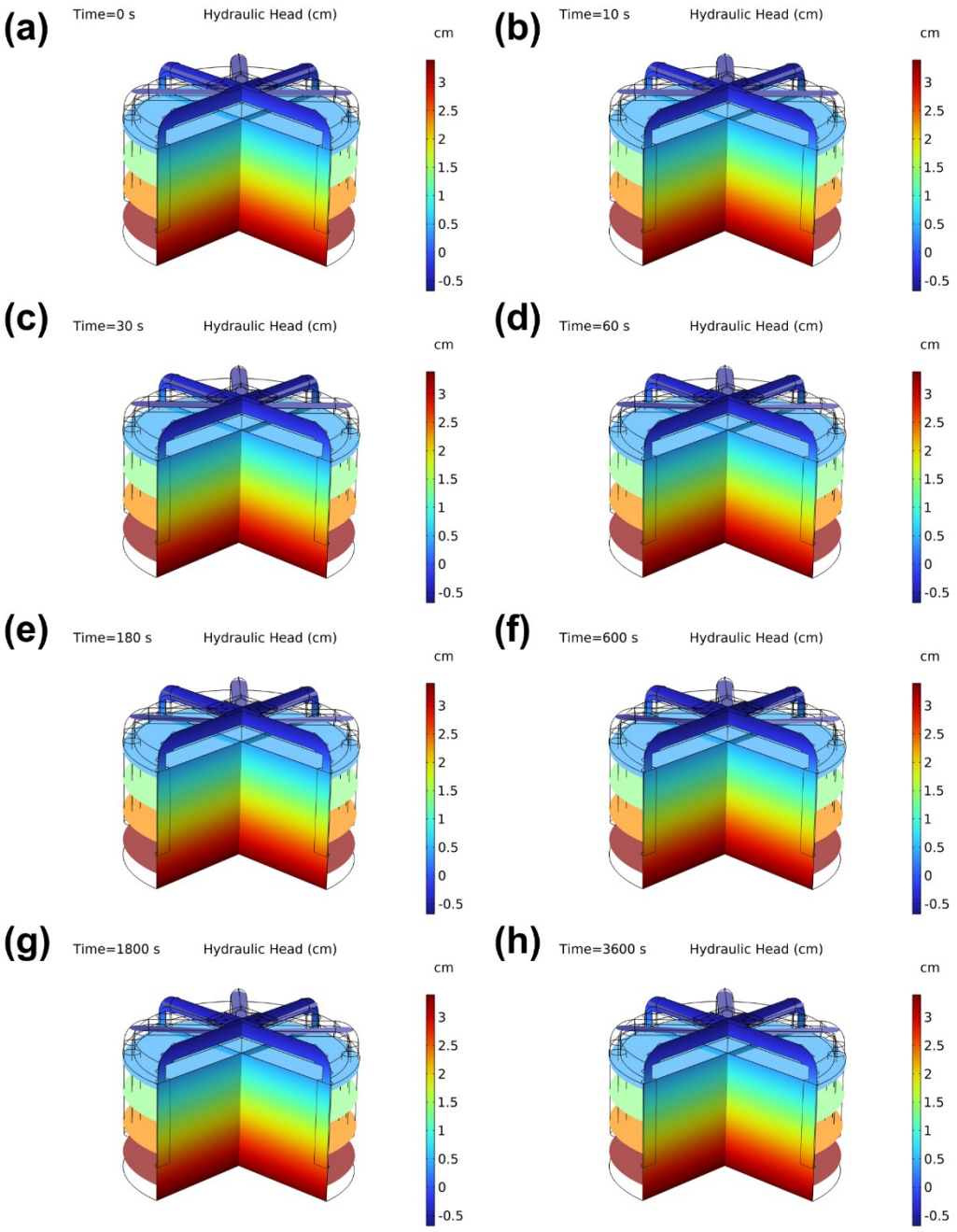

Figure S26 Transient state simulation of hydraulic head distributions at (a) 0 s, (b) 10 s, (c) 30 s, (d) 60 s, (e) 180 s, (f) 600 s, (g) 1800 s and (h) 3600 s, respectively.

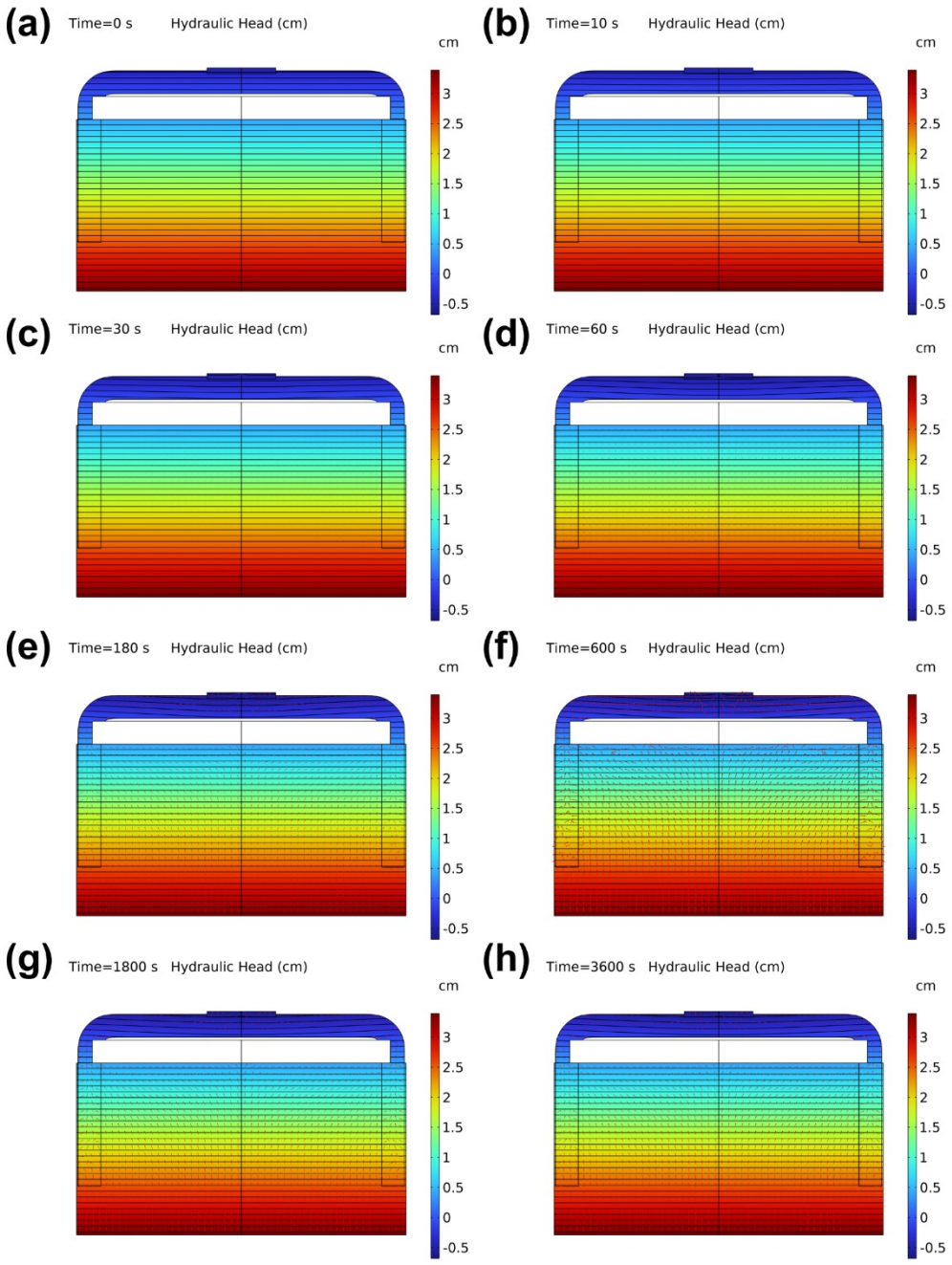

Figure S27 Transient state simulation of hydraulic head distributions at (a) 0 s, (b) 10 s, (c) 30 s, (d) 60 s, (e) 180 s, (f) 600 s, (g) 1800 s and (h) 3600 s, respectively.

Table S2 The thermal conductivity of the evaporator

Sample	Wood sponge	Sponge	Cotton	CPPB hydrogel
Thermal conductivity (W m^{-1} K^{-1})	0.30	0.32	0.28	0.36

References:

1. F. Li, N. Li, S. Wang, L. Qiao, L. Yu, P. Murto and X. Xu, Self - Repairing and Damage - Tolerant Hydrogels for Efficient Solar - Powered Water Purification and Desalination, *Adv. Funct. Mater.*, 2021, **31**, 2104464.
2. Z. Yang, H. W. Liu, J. Li, K. Yang, Z. Z. Zhang, F. J. Chen and B. D. Wang, High-Throughput Metal Trap: Sulfhydryl-Functionalized Wood Membrane Stacks for Rapid and Highly Efficient Heavy Metal Ion Removal, *ACS Appl. Mater. Interfaces*, 2020, **12**, 15002-15011.
3. L. Zhang, B. Tang, J. Wu, R. Li and P. Wang, Hydrophobic Light-to-Heat Conversion Membranes with Self-Healing Ability for Interfacial Solar Heating, *Adv. Mater.*, 2015, **27**, 4889-4894.
4. H. Zou, X. Meng, X. Zhao and J. Qiu, Hofmeister Effect-Enhanced Hydration Chemistry of Hydrogel for High-Efficiency Solar-Driven Interfacial Desalination, *Adv. Mater.*, 2023, **35**, e2207262.
5. Y. Guo, L. S. Vasconcelos, N. Manohar, J. Geng, K. P. Johnston and G. Yu, Highly Elastic Interconnected Porous Hydrogels through Self-Assembled Templating for Solar Water Purification, *Angew. Chem. Int. Edit.*, 2021, **61**, e202114074.
6. Y. Jiang, N. An, Q. Sun, B. Guo, Z. Wang, W. Zhou, B. Gao and Q. Li, Biomass hydrogels combined with carbon nanotubes for water purification via efficient and continuous solar-driven steam generation, *Sci. Total. Environ.*, 2022, **837**, 155757.
7. L. Zhang, Z. Xu, L. Zhao, B. Bhatia, Y. Zhong, S. Gong and E. N. Wang, Passive, high-efficiency thermally-localized solar desalination, *Energ. Environ. Sci.*, 2021, **14**, 1771-1793.
8. R. Niu, J. Ren, J. J. Koh, L. Chen, J. Gong, J. Qu, X. Xu, J. Azadmanjiri and J. Min, Bio - Inspired Sandwich - Structured All - Day - Round Solar Evaporator for Synergistic Clean Water and Electricity Generation, *Adv. Energy Mater.*, 2023, **13**, 2302451.